INTERNATIONAL JOURNAL FOR NUMERICAL AND ANALYTICAL METHODS IN GEOMECHANICS
*Int. J. Numer. Anal. Meth. Geomech.* (2012)
Published online in Wiley Online Library (wileyonlinelibrary.com). DOI: 10.1002/nag.2111

# Numerical modeling of fluid-driven fractures in cohesive poroelastoplastic continuum

E. Sarris[1,*,†] and P. Papanastasiou[2]

[1]*International Water Research Center (I.W.R.C) NIREAS, University of Cyprus, 1678 Nicosia, Cyprus*
[2]*Department of Civil and Environmental Engineering, University of Cyprus, 1678 Nicosia, Cyprus*

SUMMARY

In this article, we investigate the main parameters that influence the propagation of a fluid-driven fracture in a poroelastoplastic continuum. These parameters include the cohesive zone, the stress anisotropy, and the pore pressure field. The fracture is driven in a permeable porous domain that corresponds to weak formation by pumping of an incompressible viscous fluid at the fracture inlet under plane strain conditions. Rock deformation is modeled with the Mohr–Coulomb yield criterion with associative flow rule. Fluid flow in the fracture is modeled by the lubrication theory. The movement of the pore fluid in the surrounding medium is assumed to obey the Darcy law and is of the same nature as the fracturing fluid. The cohesive zone approach is used as the fracture propagation criterion. The problem is modeled numerically with the finite element method to obtain the solution for the fracture length, the fracture opening, and the propagation pressure as a function of the time and distance from the pumping inlet. It is demonstrated that the plastic yielding that is associated with the rock dilation in an elastoplastic saturated porous continuum is significantly affected by the cohesive zone characteristics, the stress anisotropy, and the pore pressure field. These influences result in larger fracture profiles and propagation pressures due to the larger plastic zones that are developing during the fracture propagation. Furthermore, it is also found that the diffusion process that is a major mechanism in hydraulic fracture operations influences further the obtained results on the fracture dimensions, plastic yielding, and fluid pressures. These findings may explain partially the discrepancies in net pressures between field measurements and conventional model predictions. 

Received 20 December 2011; Revised 10 April 2012; Accepted 3 May 2012

KEY WORDS: hydraulic fracturing; cohesive zone; net pressures; poroelastoplasticity; finite elements

## 1. INTRODUCTION

The mathematical modeling of hydraulic fracturing, which is a technique widely used in the petroleum industry to enhance the recovery of hydrocarbons from underground reservoirs, has attracted numerous research contributions over the years. A large number of studies in petroleum geomechanics have been devoted to the subject, both in an experimental and a theoretical point of view, with the main emphasis focused in the understanding of the near-tip effects. Most of the recent efforts have been oriented towards the development of numerical models to predict the propagation of hydraulic fractures in complex geological domains. However, significant contributions have also been made to understand the mathematical physics of the fluid-driven problem using rigorous and complex analysis in elastic media [1–8].

*Correspondence to: E. Sarris, International Water Research Center (I.W.R.C) NIREAS, University of Cyprus, P.O. BOX 20537, 1678 Nicosia, Cyprus.
†E-mail: esarris@ucy.ac.cy

In practice, attention is focused on the prediction of wellbore pressure, which is normally measured during the treatment and is usually the only parameter available to evaluate the operation. Classical fracturing simulators often underestimate the down-hole pressures. Survey on net pressures (difference between fracturing fluid pressure and the far-field confining stress) indicated that the net pressures encountered in the field are 50%–70% higher than the predicted ones [9]. This reason has triggered a series of dedicated studies that looked into the importance of the plastic behavior in hydraulic fracturing in weak rocks. All these studies had ignored the porous behavior of the rock deformations. It is easily understood that the mechanical response of rocks is usually complicated by elastic–plastic deformation coupled with diffusion of pore fluid. However, neglecting the porous behavior in elastic–plastic analysis represents only a first approximation to the problem.

When a fracture is driven in a saturated domain, the newly created surface of the fracture alters the stress field surrounding the body of the fracture and induces a pore pressure gradient that affects the effective stresses and the development of the plastic zones in the near-tip area of the fracture. Furthermore, the fluid-driven problem in an inelastic saturated porous media further complicates the analysis as the diffusion of the fracturing fluid through the solid introduces some rate dependency in the overall solution and behavior of the numerical model. Thus, it is necessary to develop an appropriate numerical model to further investigate the coupling of pore pressure diffusion with nonlinear rock deformation and damage criteria.

The interaction between a pore fluid and the elastic skeleton of a porous material was first developed by Biot [10] and may be considered to be a special case of the theory of interacting continua or of the theory of mixtures. Since then, the theory of poroelasticity was established. The assumption of linear elastic behavior and Darcy flow behavior of the porous skeleton that will remain unaltered during loading of a poroelastic material is recognized as a limitation of the classical theory. A natural extension to the classical theory is to introduce concepts such as elastoplasticity to account for irreversible effects in the behavior of the porous skeleton. Such extension is capable of giving rise to alterations in the elasticity and fluid flow behavior as a result of the generation of microcracks and microvoids in the porous continuum. The comprehension of these nonlinear mechanisms and the parameters affecting them is of fundamental importance in hydraulic fracturing operations as it may explain the discrepancies in net pressures between field measurements and conventional model predictions.

There are few contributions that account for the elastic–plastic behavior of fluid-saturated porous media when analyzing fracture propagation. Plastic dilatancy effects at the fracture tip were analyzed with the conduction of laboratory experiments [11] and finite element modeling [12]. Other research works presented a fully coupled model for hydraulic fracture propagation, utilizing the Mohr–Coulomb yield condition incorporated into a combined finite difference–finite element and remeshing algorithm [13–15]. Recently, from laboratory experiments, the inelastic behavior of rocks has been successfully linked with the high elevated net pressures observed in hydraulic fracturing tests [9]. Near-tip asymptotic solutions were reported with a Drucker–Prager yield condition with volumetric associative [16] and nonassociative flow law [17], with isotropic hardening to analyze steady fracture growth first in elastic–plastic without porous media and then to fluid-saturated porous mechanics.

There are few studies utilizing the cohesive zone model in hydraulic fracturing. Some early studies in this area include the important work of Boone and his coworkers [18, 19] in which they used the cohesive zone approach to model the fracture process in impermeable and permeable rocks. Other significant works include the use of the cohesive zone law to propagate fractures to investigate the inelastic behavior of rocks in hydraulic fracturing [12–15]. Improving the research work in hydraulic fracturing, a model was proposed with a tip velocity provided as part of the solution algorithm. Hydraulic fractures were successfully propagated in an unknown path that may enucleate everywhere, depending only on the stress and pressure fields [20]. More recently, research works investigated in detail the influence of the constitutive cohesive zone characteristics on the size of process zone and consequently on the obtained results in hydraulic fracturing modeling. They further demonstrated that the existence of high confining stresses influences further the size of the process zone both in elastic and poroelastic conditions [21]. In an extension of their previous works, they found that higher pressures are needed to extend a fracture in a poroelastic medium than in an elastic medium, and the created profiles of poroelastic fracture are wider. Wider fracture profiles are



DOI: 10.1002/nag

obtained with higher injection rates. The fluid pressures and the fracture apertures are larger in the case of a high permeability formation [22].

In this research work, we extend the recent work of [21, 22] to evaluate the influence of the plastic zones on the fracture and pressure behavior under poroelastoplastic conditions. The yielding mechanism used in the present work is associated with frictional sliding, either along particles or microcracks. The rock is modeled by the Mohr–Coulomb flow theory, the fracture propagation criterion used is the cohesive zone law, the fluid flow inside the fracture is described by lubrication theory, and the pore fluid movement inside the porous domain is successfully modeled with the Darcy law. With the solution of the numerical model described earlier, we have found that the cohesive zone characteristics, the stress anisotropy, and the pore pressure field result in larger fracture profiles and propagation pressures due to the large plastic zones that are developing during the fracture propagation. Furthermore, it is also found that the diffusion process that is a major mechanism in hydraulic fracture operations influences further the obtained results on the fracture dimensions, plastic yielding, and fluid pressures. These findings are important in improving the numerical simulators of modeling hydraulic fracturing in particular for short fractures in weak formations for sand control applications. The results are also important to better prediction of vertical fracture growth and containment in shale–natural gas stimulations where there are serious environmental concerns on the risk of groundwater contamination.

The body of this article is structured as follows: In the next part, we describe the involved physical processes: the fluid flow, the rock deformation, the fracture propagation, the methodology that was adopted in the numerical model, and the scaling of the plastic zones. In the second part, we present and critically evaluate the computational results and draw conclusions on the important parameters.

## 2. METHODOLOGY OF THE NUMERICAL MODEL

The physical process of the fluid driven fracture involves the pumping of a viscous fluid that pressurizes the fracture surfaces which deform. Increasing the pressurization, rock dilation will occur, and as critical loading conditions will be reached ahead of the tip, the rock will split and the fracture will be driven hydraulically. Thus, this process reveals that there is a strong coupling between the moving fluid, rock deformation, and fracture propagation, as shown in Figure 1.

Depending on the formation properties, *in situ* stresses, and pumping parameters, the fracture may propagate for more than hundred meters. In this study, the fracture will propagate a few meters, enough to extrapolate and reach correct conclusions for long fractures. The propagation of a short fracture can also be used to interpret the results of the mini-frac calibration test that is carried out first *in situ* for determining parameters such as the formation permeability and the closure stress, which are further used for modeling the long hydraulic fractures [21].

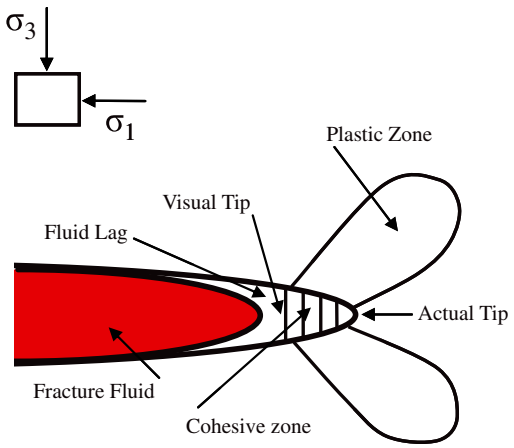


Figure 1. Geometry of a plane strain fracture driven in inelastic porous formation.



DOI: 10.1002/nag

In this research work, the objective was to investigate the main parameters influencing the development of plastic zones in a porous–plastic rock under fully saturated conditions. Fluid loss, which is also considered, is allowed from the fracture walls (permeable walls) into the rock through diffusion. This leak-off is treated as unidirectional (one-dimensional), and the scope is to investigate any effects associated with the coupled processes such as changes in the deformation due to diffusion of pore pressure or flows and pressures induced by mechanical deformation. Another important feature of the model is that the fluid flow surrounding the tip zone and the bulk of the fracture is capable of generating backstresses that cannot be ignored in hydraulic fracture operations as these nonlinear mechanisms are capable of generating excessive pore pressures or altering the fluid characteristics of the fracturing fluids. Furthermore, they may explain the differences observed in net pressures between field measurements and model predictions.

In this section, we describe the fully coupled numerical model for a fluid-driven fracture in a poroelastoplastic rock that has been used to study the importance of the plastic zones and the cohesive zone characteristics in hydraulic fracturing. The models were developed for plane strain geometry, taking into consideration the symmetry conditions. This geometry is appropriate for modeling short fractures, with fracture height relatively greater than the fracture length. Furthermore, this geometry is also appropriate for examining tip effects because the deformation of any arbitrary fracture shape is approximately planar near the tip. The fracture propagates perpendicular to the minimum *in situ* stress and remains planar. This predefined path for the propagation is also convenient with the cohesive zone numerical approach [14, 15, 21].

The model is based on the fundamental assumption of the fully symmetric description of the fracture, which one may argue is unrealistic. Experimental results [23] have shown that cross-sections of a fluid-driven fracture exhibit very complex geometry. As fractures may form from several overlapping of microfractures and bridges are linking the two fracture faces, three-dimensional effects may also be responsible for explaining high breakdown pressures and must be taken into account [23]. The cohesive zone approach implemented in this study takes into account implicitly the development of unconnected microfractures at the area of the process zone. Microcracks in shearing mode are homogenized and modeled implicitly by the plastic zones, which are developed around the fracture tip. The detail how these microcracks interact and coalesce to form the complex branching shape and system of fractures is not claimed to be investigated. Furthermore, the model formulated for the purposes of this analysis is for a two-dimensional continuum medium and does not describe fully three-dimensional effects, which may probably explain a part of high net pressures for low-porosity rocks. In other words, the only limitation of this model is the nonexplicit modeling of three-dimensional effects. The different types of rocks for which the model can be applied are taken into account with the appropriate choice of constitutive parameters for both the yield criterion and the cohesive zone.

### 2.1. *Fluid flow*

The fluids that are used for pressurizing the fractures are normally power law with shear-thinning behavior, which means that the viscosity decreases with increasing shear strain rate. To avoid this complex fluid behavior, the simplest appropriate model for fluid flow in a fracture is embodied in lubrication theory. It assumes laminar flow (uniformly viscous Newtonian), the fluid is incompressible, and it accounts for the time-dependent rate of the fracture opening. The continuity equation, which imposes the conservation of mass in one-dimensional flow, is as follows:

$$\frac{\mathrm{d}q}{\mathrm{d}x} - \frac{\mathrm{d}w}{\mathrm{d}t} + q_i = 0 \tag{1}$$

where $q$ is the flow along fracture length $x$, $q_i$ is the fluid loss in rock mass, and $w$ is the fracture opening. Equation (1) accounts for the fluid leak-off from the fracture surface into the rock formation.

The second equation is derived from the conservation of momentum balance. For a fluid flow between parallel plates, the lubrication equation, which relates the pressure gradient to the fracture width for a Newtonian fluid of viscosity $\mu$, yields to



DOI: 10.1002/nag

$$q = u.w = -\frac{w^3}{12\mu}\frac{\mathrm{d}p}{\mathrm{d}x} \tag{2}$$

where $p$ denotes the fluid pressure and $u$ is the average velocity of the fluid on a cross-section in the fracture. At this point, the effective channel viscosity $\mu^*$ can be defined related to the fluid viscosity through the relation $\mu^* = 12\,\mu$. Equation (2) determines the pressure profile along the fracture from the local width and local flow rate. The pressure gradient is very sensitive to fracture width, according to Equation (2), therefore, the largest part of the pressure drop takes place within a small area near the tip, where the width decreases significantly before it vanishes at the tip.

The type of flow constitutive response is a tangential and normal flow along the fracture walls. The numerical model for the fluid flow is constructed for the complete length of the predetermined fracture path. There is one-to-one correspondence between the plane strain flow and domain elements at the corner nodes along the fracture path, ensuring that the fluid mass is conserved across their surface. For the numerical solution, we define a nominal small initial width and a small initial length as initial conditions. The fracturing fluid is assumed to be incompressible, and the flow boundary condition is imposed at the fracture inlet to meet the specific injection or flow rate (Neumann boundary condition). Generally, the pressure along the fracture is not known *a priori*, and it is a part of the solution. Furthermore, with the formation of a fluid lag or the use of the cohesive model, we avoid the pressure singularity at the tip where the width falls to zero. The position of the fluid front is defined by the mass conservation in the fracture.

There are two types of coupling that can occur along the fracture, depending on whether the fracture walls are assumed permeable or impermeable. For impermeable walls, the fluid pressures in the fracture are converted to equivalent nodal loads and applied appropriately. For permeable walls, the fluid pressure in the fracture must be applied as a pore pressure and a total stress boundary condition.

To complete the description of the porous medium, it is necessary to describe the equation that governs the flow within the porous skeleton. For the movement of the fluid with respect to the solid, we assume that the diffusion of pore fluid obeys the Darcy law. This classical transport law for isotropic porous media relates $q$ to the gradient of the fluid pressure $p$ according to Equation (3):

$$q = -\frac{k}{\mu}(\nabla p - f) \tag{3}$$

where $q$ is the fluid flux, $k$ is the intrinsic permeability (assumed to be constant), $\nabla$ is the gradient operator, and $f$ are the fluid volume forces. Note that we assume that the fluid in the fracture is identical rheologically to the pore fluid.

### 2.2. *Rock deformation*

For rocks that exhibit inelastic behavior, inelasticity is a function of the material parameters and loading conditions. In the near-tip area of the fracture, because of the high stress concentration that occurs, solutions from Linear Elastic Fracture Mechanics (LEFM) cannot be used to analyze the fracture process. Therefore, it is necessary to incorporate plasticity and poroelastoplasticity to properly describe the irreversible deformation due to excessive shear stresses around the fracture tip and to use a nonlinear fracturing criterion.

For the inelastic response of the porous medium, the material model that has been adopted in the numerical calculations is formulated in the spirit of the Mohr–Coulomb plasticity with associated flow rule. The Mohr–Coulomb criterion is given by

$$f = \frac{1}{2}(\sigma_1 - \sigma_3) + \frac{1}{2}(\sigma_1 + \sigma_3)\sin\varphi - c\cos\varphi \tag{4}$$

where $c$ is the material cohesion and $\varphi$ is the material friction angle. The sign convention adopted here is according to classical mechanics, that is, compression is negative. The Mohr–Coulomb criterion, unlike the Drucker–Prager criterion, assumes that failure is independent of the value of the intermediate principal stress. However, the failure of typical rock-like and soil-like materials includes small dependence on the intermediate principle stress, which will be neglected in the present study.



DOI: 10.1002/nag

Having established the yield criterion is now necessary to define a relationship, the so-called flow rule for generating plastic strains in the postyielding behavior of the material. The plastic potential function $g$ is defined as

$$g = \frac{1}{2}(\sigma_1 - \sigma_3) + \frac{1}{2}(\sigma_1 + \sigma_3)\sin\psi \tag{5}$$

where $\psi$ is the dilation angle. The dilation angle $\psi$ and the material friction angle $\varphi$ could be both functions of the plastic strain history in hardening models. In this study, we assumed that the dilation angle is equal with the friction angle, $\psi = \varphi$; hence, the plastic potential function $g$ is identical to the yield function $f$ as for associated plasticity. It should be noted that the considered associated flow rule returns maximum plastic dissipation only for elastic-perfectly plastic materials and might not give maximum plastic dissipation for many types of hardening materials. However, this rule is found to closely capture the true behavior for a variety of materials.

In examining the porous behavior of the rock, the Biot poroelastic theory was reformulated in a more physically relevant manner to account for poroelastic effects by Rice and Cleary [24]. For the definition of a poroelastic system, five material constants are required. These material constants include the drained shear modulus $G$, the drained Poisson ratio $v$, the undrained Poisson ratio $v_u$, the Skempton's pore pressure coefficient $B$, and the intrinsic permeability $\kappa$ (Darcies). Rice and Cleary [24] have successfully linked these constants to micromechanical parameters that can be easily obtained for any soil- or rock-type material. These micromechanical parameters are the porosity $n$, the fluid bulk modulus $K_f$, the solid grain bulk modulus $K_s$, the porous bulk modulus for the solid skeleton $K$, the Poisson ratio $v$, and the permeability $k$. The total stresses $\sigma_{ij}$ are related to the effective stresses $\sigma'_{ij}$ through:

$$\sigma_{ij} = \sigma'_{ij} - ap \tag{6}$$

where $p$ is the fluid pressure. The effective stresses govern the deformation and failure of the rock. The poroelastic constant $a$ is independent of the fluid properties, and it is defined as

$$\alpha = \frac{3(v_u - v)}{B(1-2v)(1+v_u)} = 1 - \frac{K}{K_s} \tag{7}$$

As it is mentioned previously, this theory is commonly applied in soils. An important distinction when applying this formulation to rock is to consider the compressibility of the constitutive materials. For soils, $B$ and $\alpha$ are equal to unity but in rocks are significantly less than 1.

In conventional rock mechanics, failure of rock formations is analyzed for dry domains (i.e., no pore pressure acting in the system). However, the usual assumption when analyzing failure of rocks in poromechanical systems is that the rock is saturated. Because the formations in petroleum-related rock mechanics are generally saturated, this assumption is quite valid, and it is important to investigate how the saturation affects the failure process. It is known that failure is governed by the effective stresses. In this case, the failure criterion must be modified to account the fluid pressure constrain. The failure criterion for a formation with pore fluid pressure is obtained by introducing the effective stress into the dry form of the failure criterion. The Mohr–Coulomb theory and the equation describing failure in porous conditions are modified as [25]:

$$\sigma_1 - p_f = 2c\frac{\cos\varphi}{1-\sin\varphi} + (\sigma_3 - p_f)\frac{1+\sin\varphi}{1-\sin\varphi} \tag{8}$$

where $\sigma_1$ is the maximum *in situ* stress, $\sigma_3$ is the maximum *in situ* stress, $p_f$ is the pore pressure acting in the system, $c$ is the material cohesion, and $\varphi$ is the material friction angle.

The only extra parameters that are needed to model the inelastic behavior of the porous continuum as described earlier are the material cohesion $c$, the material friction angle $\varphi$, and the dilation angle $\psi$, which controls the volumetric change due to yielding and dilation of the material. However, to keep the parameters to a minimum, we have assumed the associative plasticity theory, which justifies the



DOI: 10.1002/nag

equivalence of the material friction angle with the dilation angle. Furthermore, in the hydraulic fracturing problem, the initial *in situ* mean pressure in the near area of the fracture tip decreases during propagation, and under such conditions, it is reasonable to assume an associative behavior. In addition, Papanastasiou and Thiercelin [12] showed that the solution for nonassociative material lays between the solution of elastic and associative material; therefore, the elastic solution and the associative solution present the two bounds for the nonassociative case.

In summary, the rock mass remote from the fracture is initially elastic, then deforms plastically, and then unloads elastically after the fracture has advanced. Under such conditions, the poroelastoplastic model must be capable of dealing with nonproportional loading.

### *2.3. Fracture propagation*

The criterion for fracture propagation is usually given either by conventional energy approach, which states that a fracture propagates when the energy release rate reaches a critical value related to fracture toughness or by the stress intensity approach, which states that a fracture propagates when the stress intensity factor at the tip exceeds the rock toughness. The energy release rate and stress intensity approaches are essentially equivalent and uniquely related for linear elastic materials. The most robust criterion for nonlinear mechanics is described by the cohesive zone constitutive model. The cohesive zone model approach should be clearly contrasted with the conventional fracture mechanics-based infinitely sharp fracture models as such fracture models have led to a physically meaningless singular stress field near the fracture tip. The cohesive zone is a region ahead of the fracture tip that is characterized by microcracking along the fracture path. The main fracture is formed by interconnection of these microcracks. The cohesive zone model implies that normal stress continues to be transferred across a discontinuity, which may or may not be visible as shown in Figure 2. This stress is determined from the softening stress–strain relation that various rocks exhibit in calibrations tests. This transferred normal stress is a function of the separation and falls to zero at a critical opening, and then the fracture propagates.

The evolution of the fracture is governed by THE energy balance between the work of the external loads and the sum of the bulk energy of the uncracked part and the energy dissipated in the fracture process. The main mathematical difficulty is given by the fact that the fracture energy depends on the opening of the distributed microcracks. To simplify the mathematical difficulties, it is assumed that the cohesive zone localizes, due to its softening behavior, into a narrow band ahead of the visible fracture.

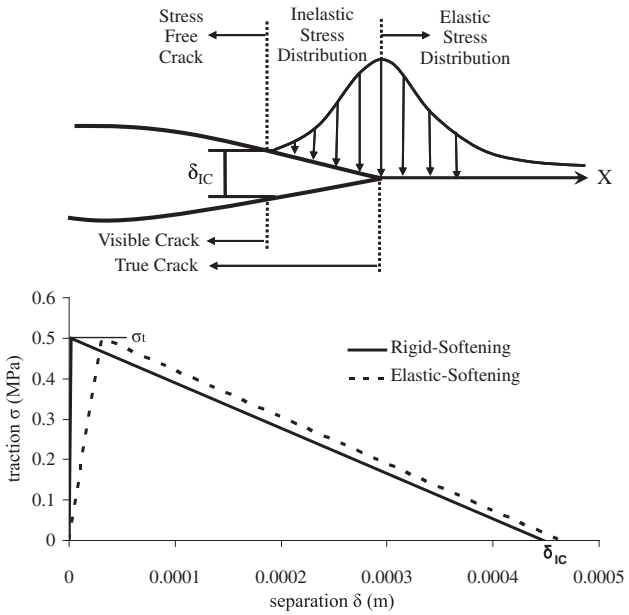


Figure 2. Representation of the fracture process and the constitutive cohesive zone law.



DOI: 10.1002/nag

The constitutive behavior of the cohesive zone is defined by the traction–separation relation derived from laboratory tests. The traction–separation constitutive relation for the surface is such that with increasing separation, the traction across this cohesive surface reaches a peak value and then decreases and eventually vanishes, permitting for a complete separation.

Simple cohesive zone models can be described by two independent parameters, which are usually, for mode I plane strain, the normal work of separation or the fracture energy $G_{\mathrm{IC}}$ and either the tensile strength $\sigma_{\mathrm{t}}$ or the complete separation length $\delta_{\mathrm{IC}}$. An additional parameter in these models is the slope of the initial loading, which may define a range from rigid softening to elastic softening response under tensile stress state. Sarris and Papanastasiou [21] examined the main characteristics of this curve by carrying out computations for different initial slopes to simulate a rigid softening to elastic softening behavior. The transition from the elastic softening to the rigid softening was carried out by increasing the initial slope of the constitutive cohesive law. They found that the most rigid behavior accurately represents the elastic case as the cohesive zone in the near fracture tip area shrinks significantly.

The area under the traction–separation curve equals with fracture energy $G_{\mathrm{IC}}$, which is the work needed to create a unit area of fully developed fracture. Rice [26] has showed that the critical value $J$ integral can be equivalent with the critical value of the fracture energy $J_{\mathrm{IC}} = G_{\mathrm{IC}}$, when the size of the cohesive zone is small compared with the fracture length. For elastic solids, this energy is related to the rock fracture toughness $K_{\mathrm{IC}}$ through [26, 27]

$$K_{\mathrm{IC}}^2 = \frac{G_{\mathrm{IC}} E}{1 - v^2} \tag{9}$$

where $E$ is the young modulus and $v$ is the Poisson ratio. The rock fracture toughness can be calculated from laboratory tests. For the case of the rigid-softening behavior, the traction–separation relation is uniquely determined by

$$\sigma = \sigma_{\mathrm{t}}(1 - \delta/\delta_{\mathrm{IC}}) \tag{10}$$

where $\sigma_{\mathrm{t}}$ is the uniaxial tensile strength of the rock and $\delta_{\mathrm{IC}}$ is the critical opening displacement at which $\sigma$ falls to zero. The value of $\delta_{\mathrm{IC}}$ is given by

$$\delta_{IC} = \frac{2K_{IC}^2(1 - v^2)}{\mathrm{E}\sigma_t} \tag{11}$$

For the case of the elastic loading, the cohesive constitutive relations were augmented and modified to take into account the initial part of the curve as follows [21]:

$$\sigma = \sigma_t\left(\frac{\delta}{\delta_{el}}\right) \tag{12}$$

with the limit of elastic deformation given by

$$\delta_{el} = \frac{\sigma_t}{k_n} \tag{13}$$

where $k_n$ is the stiffness of the traction–separation relation in the loading regime with units of MPa/m. In the post-peak softening regime, the cohesive constitutive relation is given by

$$\sigma = \sigma_t\left[1 - \frac{(\delta - \delta_{el})}{(\delta_{IC} - \delta_{el})}\right] \tag{14}$$

The assumption that the cohesive zone localizes, due to its softening behavior, into a narrow band ahead of the visible fracture is very convenient for finite element analysis, where the softening behavior can be modeled by cohesive zone elements [21, 28].



DOI: 10.1002/nag

### 2.4. Finite element formulation

The theory of poroelastoplasticity can be approximated numerically using the finite element method and a standard Galerkin formulation, as described by Lewis and Schreffler [29]. As it commonly known, this theory is commonly applied in soils, and it is identified as the second-class problem in soil–pore fluid interaction problems. An important distinction when applying the formulation to rock is that the compressibility of the constitutive materials must be considered. For soils, B (Skempton's coefficient) and $\alpha$ (Biot's coefficient) are equal to unity but in rocks are significantly less than 1. The generalized discrete finite element equations that also account for transient behavior are described by

$$\begin{bmatrix} \theta K_e & \theta Q \\ Q^T & S + \Delta t \theta H \end{bmatrix}_{n+\theta} \begin{Bmatrix} \bar{u} \\ \bar{p}^w \end{Bmatrix}_{n+1} = \begin{bmatrix} (\theta - 1)K_e & (1-\theta)Q \\ Q^T & S - 1(1-\theta)\Delta t H \end{bmatrix}_{n+\theta} \begin{Bmatrix} \bar{u} \\ \bar{p}^w \end{Bmatrix}_{n} + \begin{Bmatrix} f^u \\ \Delta t f^p \end{Bmatrix}_{n+\theta} \tag{15}$$

where $K_e$ is the elastic stiffness matrix, $Q$ is the coupling matrix, $H$ is the permeability matrix, $S$ is the compressibility matrix, $f^u$ are the forces due to displacements, and $f^p$ are the forces due to pressures. $\theta$ is the time operator that defines the type of the numerical method used to approximate the time in the equations, that is, take the values between zero and unity. Equation (15) can be decomposed into the following matrices to account for both stiffness and flow equations:

$$\begin{aligned}
B &= LN_u \quad \text{(strain operator)} \\
K_e &= \int_\Omega B^T D_e B d\Omega \quad \text{(linear elastic stiffness matrix)} \\
Q &= \int_\Omega B^T \alpha m N_p d\Omega \quad \text{(coupling matrix)} \\
H &= \int_\Omega \left(\nabla N_p\right)^T \frac{k}{\mu^w} \nabla N_p d\Omega \quad \text{(permeability matrix)} \\
S &= \int_\Omega N_p^T \left(\frac{1}{Q'}\right) N_p d\Omega \quad \text{(compressibility matrix)} \\
\frac{1}{Q'} &= \frac{a-n}{K_s} + \frac{n}{K_w} \\
f^u &= \int_\Omega N_u^T [\rho^s (n-1) + \rho^w n] g d\Omega + \int_{\Gamma_u^q} N_u^T \bar{t} d\Gamma \\
f^p &= \int_\Omega \left(\nabla N_p\right)^T \frac{k}{\mu^w} \rho^w g d\Omega - \int_{\Gamma_w^q} N_p^T \frac{q^w}{\rho^w} d\Gamma
\end{aligned} \tag{16}$$

with $N^u$ and $N^p$ being the shape functions to account the displacements and fluid pressures, respectively; $L$ is the differential operator; $D_e$ is the tangential elastic stiffness matrix; $n$ is the porosity of the solid phase; $\rho^w$ is the density of the fluid; $\mu^w$ is the viscosity of the fluid; $K_s$ and $K_w$ are the solid and fluid bulk modulus, respectively; and finally, $k$ is the intrinsic permeability.

For the linear elastic case, the constitutive relation may be expressed as a linear relation between small changes in strain and small changes in the effective stresses:

$$\delta\varepsilon = D_e \delta\sigma' \tag{17}$$

For the elastoplastic case, we need to account the irreversibility of the plastic strains. This can be included in the tangential elastoplastic stiffness matrix to account for the nonlinear behavior of the solid phase. The procedure to derive the elastoplastic stiffness matrix for any yield surface can be found in [29]. Following this procedure, we just summarize the resulting tangential elastoplastic matrix $D^{ep}$ for the Mohr–Coulomb yield surface.



DOI: 10.1002/nag

$$\delta\sigma' = \left[ D_e - \frac{D_e \left\{\frac{\partial Q}{\partial \sigma'}\right\} \left\{\frac{\partial F}{\partial \sigma'}\right\}^T D_e}{-\left\{\frac{\partial F}{\partial \varepsilon^p}\right\}^T \left\{\frac{\partial Q}{\partial \sigma'}\right\} + \left\{\frac{\partial F}{\partial \sigma'}\right\}^T D_e \left\{\frac{\partial Q}{\partial \sigma'}\right\}} \right] \delta\varepsilon \tag{18}$$

To deal with nonlinear term $D^{ep}$ in Equation (18), we need to obtain the vectors of $\left\{\frac{\partial Q}{\partial \sigma'}\right\}$, $\left\{\frac{\partial F}{\partial \sigma'}\right\}$, and $\left\{\frac{\partial F}{\partial \varepsilon^p}\right\}$. These vectors are trivially obtained through the stress invariants and some differentiation. For the elastoplastic case, the internal force vector, which is identified in the linear momentum of the porous continuum, integrates the above constitutive relation (18), resisting the elastoplastic deformation of the solid skeleton:

$$P(\bar{u}) = \int_{\Omega} B^T \delta\sigma' \, d\Omega \tag{19}$$

The equation is essential for the definition of the elastoplastic stiffness matrix, which in turn is essential for the solution of Equation (15).

### 2.5. *Scaling of plastic zones and inelasticity in the processes region*

The influence of plastic dilation on propagation pressures and fractures dimensions will depend on the size of the generated plastic zones. Due to the complexities in material model, loading conditions, and problem geometry, it is difficult to determine the exact location of the plastic zone boundaries as it is a part of the numerical solution. Therefore, an attempt is made to reach conclusions through the scaling of the most important parameters affecting the size of the plastic zones in the plastic or poroelastoplastic continua.

Based on previous research works [12, 13, 15], we have augmented the size of the plastic zones to be a function of the *in situ* stress deviator and the fluid pressure acting in the porous matrix through

$$\ell_p \propto \frac{\sigma_1 - \sigma_3}{\sigma_1 + \sigma_2 + \sigma_3 - 3P} \tag{20}$$

According to Equation (20) yielding is not expected to occur when the fracture is to propagate in a hydrostatic stress field. However, in deep rock formations, a highly nonhydrostatic stress filed is encountered due to significant stress difference between vertical and horizontal stresses for a vertical growth of the fracture. It is then clear that with increase of the *in situ* stress difference, the plastic zones will increase. Equation (20) suggests that larger plastic zones will be generated with increasing formation pore pressure.

In this research work, we investigated all the mentioned characteristics (influence of stress deviator and formation pressure) that affect the plastic zone development according to the augmented Equation (20) that describes the plastic zone scaling by conducting parametric analysis in a poroelastoplastic model to determine the influence of the pore pressure parameter on the aforementioned scaling.

The inelastic processes in the cohesive region were discussed by Shet and Chandra [30]. According to their work, the position of the cohesive fracture tip is taken to coincide with the peak traction in the cohesive zone law. This selection facilitates a part of the cohesive energy to be dissipated in the forward region of the fracture, whereas the rest of the energy is to be dissipated in the wake region. The conditions prevailing in the process zone will vary according to the type of material, geometric, and loading conditions. Fracture growth is generally promoted by dissipation, resulting from microstructural damage mechanisms in the forward region, both in the bounding material and the cohesive zone, whereas fracture advancement is impeded by other dissipation mechanisms. However, both physical processes consume energy, part of it being dissipated into the material and the rest into the fracture within the cohesive zone.

In this work, to accurately describe the fracture process in weak rocks, we model the plastic yielding that may occur in the surrounding fracture and tip area, which interacts with the mode I cohesive zone ahead of the tip. This is interpreted that in the fracture-toughness-dominated regime of a fluid-driven fracture, the energy dissipation will include the inelastic processes taking place in the whole process zone.



DOI: 10.1002/nag

## 3. NUMERICAL IMPLEMENTATION

The governing equations were discretized in space with the finite element method and in time with the finite difference method. Linear interpolations were used for the approximation of both displacement and the pore pressure degrees of freedom. The sharp changes that are expected in the geometry of the propagating tip are dealt with placing a sufficient fine mesh around the predefined fracture path so as to ensure numerical accuracy. For the numerical approximation of the aforementioned set of equations, the direct solution of the coupled systems was used. No specialized numerical techniques such as the partitioned-type numerical solution, is needed. Instead, the direct approach is selected because of its rapid convergence even in severely nonlinear cases. The time integration operator in the pore fluid flow equation is chosen to be the simple one-step method. In fact, to ensure numerical stability for the solution, we choose backward difference scheme ($\theta = 1$) to approximate the time-dependent effects in the problem. Equations are solved using the Newton method for flow problems. Equations (15)–(19) form the basis of the iterative solution in a coupled flow-deformation solution. They are, in general, nonsymmetric. The lack of symmetry may be due to a number of effects: changes in geometry, dependence of permeability on void ratio, and inclusion of fluid gravity load terms in total pore pressure analyses.

The calculations were carried out in Abaqus [31], a nonlinear finite element code suit of programs. The usual four-node, plane strain, isoparametric elements were used to model the domain and six-node cohesive elements to model the fluid flow in the fracture and the fracturing process. Both types of elements, additionally from their $u$, $v$ translation degrees of freedom (d.o.f), are equipped with a pore pressure d.o.f. to account for the fluid diffusion in the porous domain. The two additional nodes in the cohesive elements, positioned in their center, are used to simulate the fluid flow during the propagation.

The cohesive zone approach cancels the stress singularity when the separation at the tail of the cohesive zone law reaches a critical value at which the cohesive traction vanishes. Furthermore, this cancels the coupled fluid pressure singularity that is encountered in the analytic framework of the fluid-driven problem. Sinclair [32] showed that the cohesive traction–separation laws cancel the opening singularity produced by loading remotely from the fracture with the closing singularity produced by cohesive stresses on the fracture flanks near the fracture tip.

The discretized domain was considered to be $30 \times 30$ m, and the predefined path of the fracture was defined to be 11 m only (cohesive elements) to save computational time. If a longer fracture is required, it can be easily implemented by extending the cohesive elements to the desired fracture length. The wellbore location is at the left lower corner, and the fracture is assumed to grow in both directions along the $x$ axis. For a long fracture, the size of the wellbore is negligible and is usually ignored in the modeling. This remark, along with the condition that the wellbore is cased, cemented, and fully bonded with the rock formation, justifies the use of symmetry conditions within a reasonable accuracy.

Symmetry conditions were imposed at the bottom ($dy = 0$, fixed displacements) and at the left ($dx = 0$, fixed displacements) side of the models. The *in situ* stresses were generated as initial stresses and by applying the equilibrium load at the far end edges. At the top edge, the value of $\sigma_3$ (MPa) was considered as the minimum *in situ* stress, and at the right side of the models, the value of $\sigma_1$ (MPa) was considered as the maximum *in situ* stress; these stresses are shown in Table I, and their influence was studied in detailed, as it will be described later. An initial condition is also required for defining an initial fracture length for the flow. This length was considered 0.1 m, which is approximately equal with the perforation length to obtain a well-posed system with appropriate conditions. The *in situ* stresses and the initial conditions are applied in the first step to achieve system equilibrium before the propagation steps.

## 4. COMPUTATIONAL RESULTS

In this section, we present the results from the analysis of the fluid-driven problem in a poroelastoplastic solid to demonstrate the fully coupled solution. The input parameters in which the numerical computations were performed are given in Table I. These parameters include the rock properties, the pumping parameters, the *in situ* stress field, and the initial conditions. The only extra parameters that are needed to consider porous deformation and propagation of the poroelastoplastic



DOI: 10.1002/nag

Table I. Input parameters and material properties.

| Variable | Value | | |
|---|---|---|---|
| Elastic rock properties | | | |
| Young modulus, $E$ (MPa) | 16 200 | | |
| Poisson ratio, $v$ | 0.3 | | |
| Inelastic rock properties | | | |
| Material cohesion, $c$ (MPa) | 1.515 | | |
| Material friction angle, $\varphi^0$ | 28 | | |
| Material dilation angle, $\psi^0$ | 28 | | |
| Cohesive zone properties | | | |
| Constitutive thickness | 1 | | |
| Anti-plane thickness | 1 | | |
| Maximum traction, $\sigma_t$ (MPa) | 0.5 | | |
| Cohesive stiffness, $k_n$ (MPa) | 81E + 3 | 162E + 3 | 324E + 3 |
| Cohesive energy, $J_{IC} = G_{IC}$ (kPa m) | 0.112 | | |
| Permeability coefficients *qt/qb* (m/s) | 2.421E – 10 | | |
| Pumping parameters | | | |
| Viscosity, $\mu$ (kPa s) | 0.0001 | | |
| Injection rate, $q$ ($m^3$/s m) | 500E – 6 | | |
| Domain permeability, $k$ (m/s) | 2.421E – 10 | | |
| *In situ* stress field (effective stresses) | | | |
| $\sigma_1$ (MPa) | 14 | | |
| $\sigma_2$ (MPa) | 9 | | |
| $\sigma_3$ (MPa) | 3.7 | | |
| Initial conditions | | | |
| Void ratio, $e$ | 0.333 | | |
| Initial gap (perforation) (m) | 0.1 | | |
| Pore pressure, $p$ (MPa) | 0.85 | 1.85 | 2.85 |

fracture are the pore pressure of the domain requiring an extra degree of freedom at the nodes of the plane strain elements and the material cohesion $c$ and friction angle $\varphi$.

To avoid any confusing results, the total stress field was applied in the analysis, and for the constitutive cohesive law after the first investigation, the elastic softening ($k_n = 5$) curve was maintained, which is considered the case where the cohesive zone that is created is the largest. $k_n$ (MPa) is the cohesive stiffness and represents the elastic part of the constitutive law. Previous research works that examined the influence of the cohesive zone in hydraulic fracturing were reported earlier in [21]. The properties of the cohesive zone are summarized in Table I. These properties include the uniaxial tensile strength, the fracture energy which is the area under the traction–separation curve calculated to meet an equivalent fracture toughness of 1 MPa.$m^{1/2}$ and the parametrically investigated loading slope of the first branch of the cohesive constitutive law.

To investigate the influence of the plastic zones in hydraulic fracturing, we have performed a number of parametric studies that will be described in the following. These studies include (i) mesh dependency check, (ii) the influence of the cohesive constitutive law, (iii) the influence of the formation pore pressure, (iv) the influence of the *in situ* anisotropic stress field according to Equation (20), and finally (v) the reduction of the fluid-saturated poroelastoplastic problem to the dry porous elastoplastic problem.

According to Papanastasiou [14], the analysis of the fluid-driven fracture propagating in nonporous formation with a yield criterion to capture plastic yielding and dilation effects requires fine mesh near the tip to capture the strong gradients. He incorporated a remeshing algorithm to deal with this requirement. However, in the present work, no special remeshing algorithm was used as the mesh was constructed sufficiently fine along the predefine path of the fracture.

Furthermore, a mesh dependency exercise was performed. We present a comparison between a fine mesh (solid line) and the mesh that has been used throughout the numerical computations (dashed



DOI: 10.1002/nag

line). For the case of the fine mesh, about 350 000 elements with 1 169 554 d.o.f. were constructed in the $30 \times 30$ m geometrical domain. For the case of the coarse mesh, about 15 000 elements with 49 686 d.o.f. were constructed for the same geometric domain. The aforementioned numbers show that the fine mesh has 20 times larger d.o.f than that of the coarse mesh and, therefore, is expected to be much more computationally intensive. All the results presented next correspond to fractures at the state of propagation.

Figure 3 presents a comparison of the fracture profiles between the fine and the coarse mesh. The fracture was left to reach 6 m in length in both cases. For the fracture to propagate up to 6 m in length with the coarse mesh, only 7 hours was needed, whereas for the fracture driven with the fine mesh, 6 complete days was needed. The computations were performed in a workstation with four processors and a total 8 Gb of memory. The results of Figure 3 show that only a 2.2% difference exists in the fracture profiles.

Figure 4 presents the fluid pressures needed to propagate the fractures with a fine and a coarse mesh. It is seen that the influence of the mesh dependency has a limited effect on the fluid pressures. A closer examination of the fluid pressures at 5 m shows that a 0.09% difference exists only in the fluid profiles. Taking into account the computational time efficiency, the analyses were chosen to be performed with the coarser mesh.

Figure 5 shows the obtained half width of fractures propagating in a poroelastoplastic domain for cases of different loading slopes of the cohesive constitutive relation. The fracture length of 2 m is relative short so any conclusion is associated with near wellbore fractures. In the poroelastoplastic hydraulic fractures, the process zone includes the generated plastic zones. We see that the calculated width of the propagating fracture that corresponds to the elastic softening case ($k_n \times 5$) is much larger than the calculated width of the rigid softening, which corresponds to $k_n \times 20$. Furthermore, it is seen that the cusping of the fracture profile is larger in the case of $k_n \times 5$.

This large cusping is explained by the fact that in the elastic-softening case, the cohesive tractions are effective in resisting the fracture growth, leading to more open fractures. This is also in agreement with the research work of Zuorong *et al*. [33], although in their work, they considered elastic fractures.

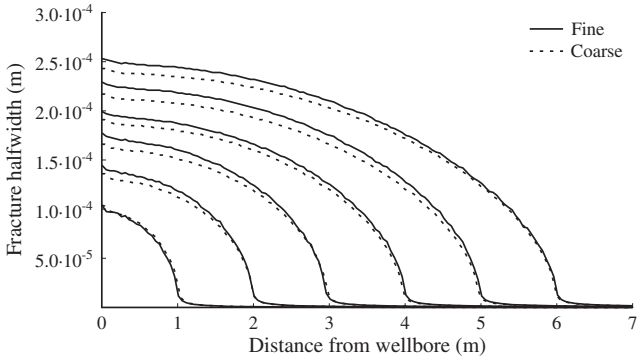


Figure 3. Comparison of fracture profiles between coarse and fine mesh in a poroelastoplastic analysis.

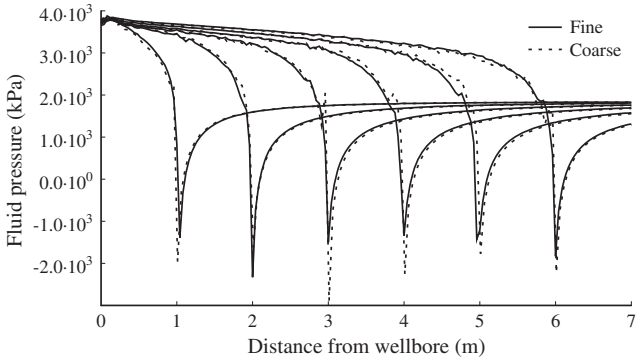


Figure 4. Comparison of fluid pressures for coarse and fine mesh in a poroelastoplastic analysis.



DOI: 10.1002/nag

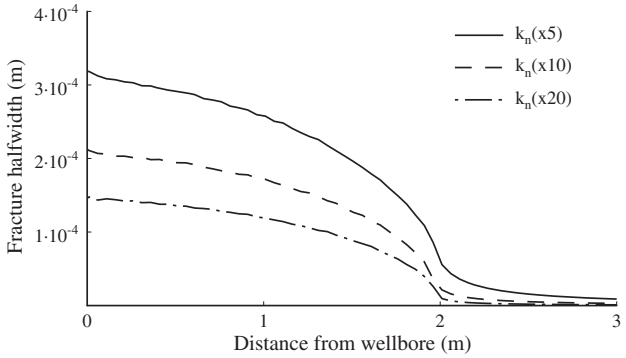


Figure 5. Fracture apertures for different values of the loading slope of the constitutive cohesive zone law.

Figure 6 shows the corresponding pressure profile in the fractures when the visual tip has reached the distance of 2 m. The fluid front position is found to be where the fluid pressure changes sign.

It was assumed in these computations that the fluid reaches the fracture visual tip. From the fluid pressure profile, it is evident that the fractures that correspond to the case of $k_n \times 5$ demand higher pressures to propagate. Another important feature of Figure 6 is that the pore pressure field that is observed in front of the visual tip is influenced by the fracture process. This behavior is explained by the local volumetric strain that is caused by material yielding and the different size of the process zone, which includes the plastic zones.

Figure 7 shows the net breakdown pressure of the formation and the net propagation pressure. The initiation pressure is significantly larger in the case of $k_n \times 5$ and tends asymptotically to a constant value after some propagation distance away from the wellbore. The pressures during early times of

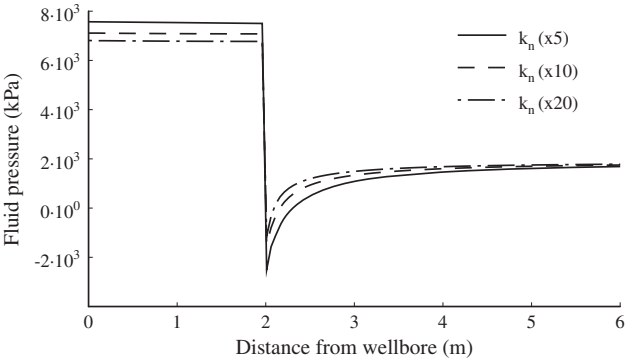


Figure 6. Fluid pressures in the fractures for different values of the loading slope of the constitutive cohesive law.

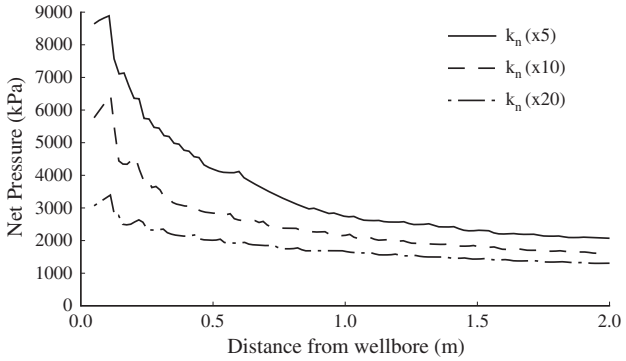


Figure 7. Net pressures versus fracture length for different values of the loading slope of the cohesive zone law.



DOI: 10.1002/nag

injection are initially increasing for some propagation steps until the stress field and cohesive zone, which includes the plastic zones, are fully developed.

After the first few propagation steps, the net pressures tend to decrease to a certain steady-state value. This can be explained by the fact that the effect of the cohesive zone in the poroelastoplastic continuum is highly significant near wellbore, but as the fractures propagate away from the wellbore, this effect becomes weaker because the size of the process zone becomes negligible compared with the fracture length.

A small discrepancy exists in the physical meaning of the fracture-toughness-dominated regime ($K$-dominant) between the poroelastic and the poroelastoplastic solutions. The physical meaning of the fracture-toughness-dominated regime in the poroelastic cases is that the effective fracture toughness increases, and significant amount of energy is expended in fracturing the material. The effective fracture toughness can be calculated from the $J$-integral approach, which successfully assumes this $K$-dominant region ahead of the fracture tip. In this region ahead of the fracture tip, the stress and displacement fields are a function of the loads and the fracture length. Therefore, the fracture-toughness-dominated regime in the poroelastoplastic fracture can only exist when the inelastic region can be contained within an angular region surrounding the fracture tip, which means small scale yielding [15, 27]. In the poroelastoplastic case if plastic yielding is large, the condition of the fracture toughness dominated regime may lose its meaning.

At this point, the basic assumption of the cohesive zone that it is localized in a narrow band ahead of the fracture tip may still be valid as the plastic yielding (plastic zones) of the material interacts with the more localized deformation in the cohesive zone. This means that the plot of the cohesive stresses versus distance from visual tip will not be representative for the size of the process zone, which includes the surrounding plastic zones. To obtain a measure of the process zone, the energy that is dissipated due to plastic yielding is calculated.

Figure 8 presents a measure of the plastic zones that are generated (plastic energy dissipation) in the numerical model versus propagation time. The energy that is dissipated due to plasticity (Joules) is calculated for the entire numerical model from the following equation, which is derived from the internal energy balance.

$$E_{\mathrm{p}} = \int_0^t \left( \int_V \sigma : \dot{\varepsilon}^{\mathrm{pl}} \mathrm{d}V \right) \mathrm{d}t \tag{21}$$

Figure 8 shows that larger plastic zones are created for the case of $k_n \times 5$ as a result of the higher energy that is dissipated due to plasticity. Initially, the energy is exponentially dissipated as a result that for early times of injection, the cohesive zone that includes the plastic zones is developing, and after the first propagation steps, it continues in a linearly increasing manner. It is also seen that more time is needed to propagate the fracture to the same extent (i.e., 2 m) for the case of $k_n \times 5$ due to the larger volume of the created fracture.

The size and boundaries of the plastic zones are shown by the contours of the plastic equivalent strains that are plotted in Figure 9 for the representative case of a propagating poroelastoplastic fracture in soft

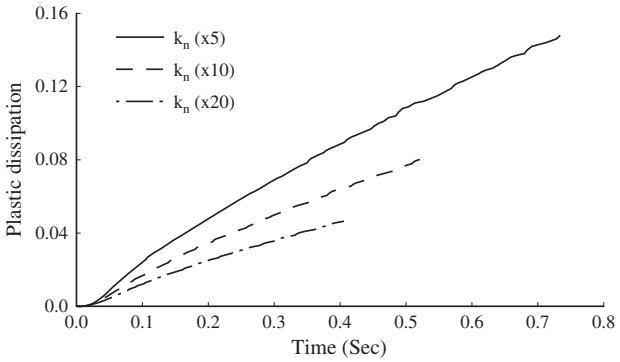


Figure 8. Plastic dissipation versus time for different values of the loading slope of the cohesive zone law.



DOI: 10.1002/nag

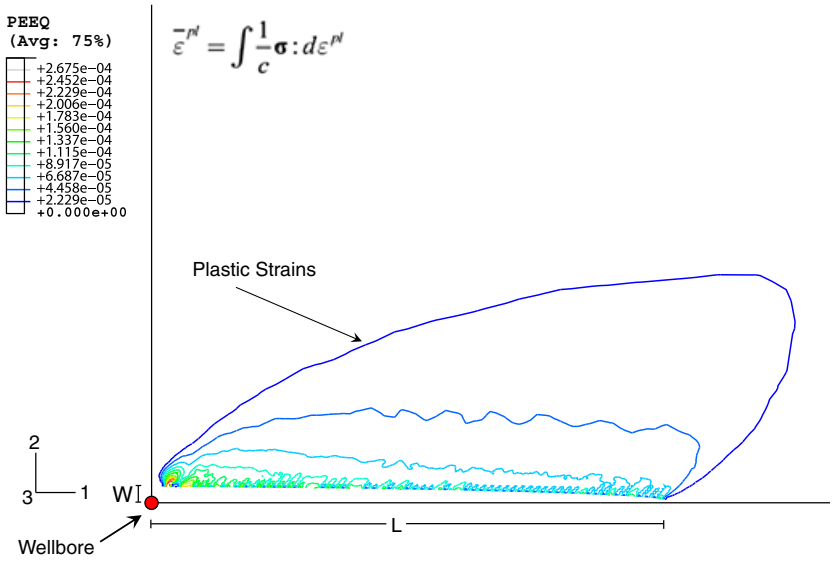


Figure 9. Contours of equivalent plastic strain.

$k_n \times 5$ formation. The definition of the equivalent plastic strain for the Mohr–Coulomb failure criterion is given by

$$\varepsilon^{\mathrm{pl}} = \int \frac{1}{c}\sigma : d\varepsilon^{\mathrm{pl}} \tag{22}$$

where $c$ is the cohesion yield stress. Figure 9 is plotted after the fracture has been left to propagate up to 2 m length (i.e., $L = 2$ m). The strain contours extend in significant distance from the fracture surfaces into the formation. The equivalent plastic strain contours show the large plastic zones that are created for a propagating fracture in soft rock formation. For a short fracture, this plastic zone is considered large, but it relatively decreases as the fracture propagates longer.

High-intensity yielding is observed near the tip, and residual plastic strain accumulates near the fracture walls after material unloading behind the advancing tip as the fracture propagates. As the fracture propagates, the plastic yielding reaches steady state conditions.

Figure 10 is a contour plot of the pore pressure field for representative case of propagating poroelastoplastic fractures in soft $k_n \times 5$ rock formation. A highly negative regime of pore pressure exists ahead of the fracture tip, which turns highly positive just after a small distance from the fracture tip towards the wellbore. It is reminded that the domain is fully saturated, and the fluid rheology of the fracturing fluid and the formation fluid are of the same nature (incompressible Newtonian). The negative sign suggests the presence of the cohesive and dilatant regions, which enforce suction (negative values of fluid pressures) in the area of the fracture tip. In such case, the negative sign implies that fluid is pulled towards the fracture tip, which acts as a sink, and suction takes place. Just after the suction, the fluid returns to the porous domain [36]. The positive sign suggests that the fluid is directed away from the fracture walls. In other words, negative sign implies that flux is directed towards the tip and positive sign implies that flux is directed away from the fracture.

These findings are in agreement with other related works [17, 34]. Furthermore, we observed that the fluid has diffused to a large distance in the soft rock formation. As the magnitude of the negative sign is larger near the tip area, this would imply that the flux of pore fluid towards the tip is higher. This increased flux, which is sucked into the fracture and immediately returned to the porous domain, and the diffusion process increases. This means that the plastic dilation increases the flux towards the fracture tips, and the diffusion process is enhanced, rising to the creation of backstresses. The conclusion that plastic dilation triggers the flux towards the fracture tip is very similar to that of strain localization. It is known that shear bands, which are zones of high shearing and dilatancy, attract pore fluids [34]. At this point, it is important to mention that we do not model



DOI: 10.1002/nag

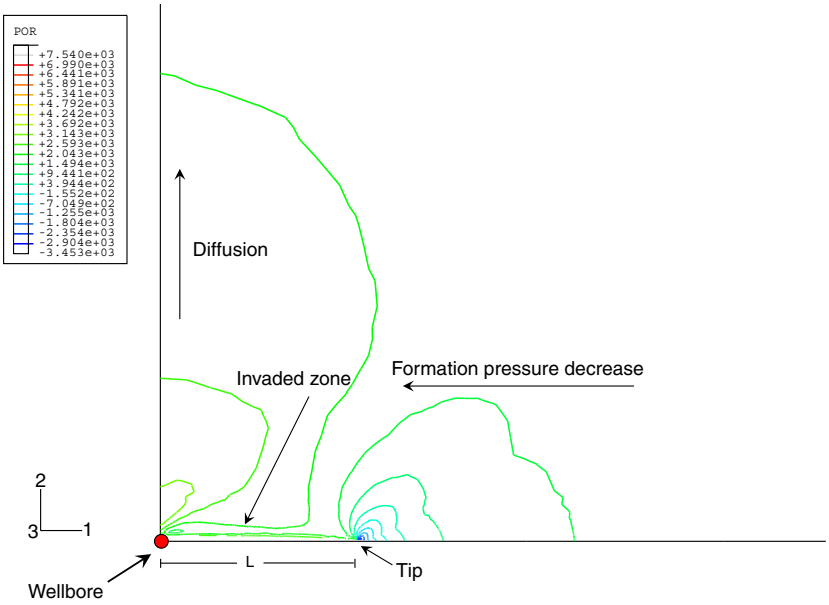


Figure 10. Contours of pore pressure for fracture tip at 2 m.

changes of permeability with deformation of the porous continuum. Here, only the diffusion process is investigated, and it is found that after enhancing the diffusion process, backstresses are created.

The next step of this research work was to investigate the influence of the stress field in a poroelastoplastic continuum according to Equation (20), which scales the plastic zone development through the *in situ* stress deviator ($\sigma_1$–$\sigma_3$). It is important to impose the stress field relatively to the fracture propagation direction. Figure 11 presents the orientation of the fracture tips with respect to the *in situ* stresses. It is generally accepted that the fracture always propagates perpendicular to the minimum *in situ* stress $\sigma_3$. In the first case shown in Figure 11, the *in situ* stress field is such that plastic yielding takes place in the plane of deformation. This corresponds to the case of a fracture that propagates vertically along the direction of the maximum *in situ* stress.

In the other case, the fracture propagates horizontally with the vertical stress, which is the maximum, to act perpendicular to the in-plane strain deformation.

The problem of the plastic zone scaling is reduced in the investigation of the value of the stress deviator as it is one of the parameters that mainly control the plastic zones. We investigated the influence of the transition from isotropic to highly anisotropic stress field on the plastic zone development. Furthermore, it is ensured that the closure stress will be kept the same so that any increase in the fracture dimensions will be attributed to the inelastic processes. For the purposes of the analysis, five stress ratios $\sigma_1/\sigma_3$ have been created to accurately capture the transition from

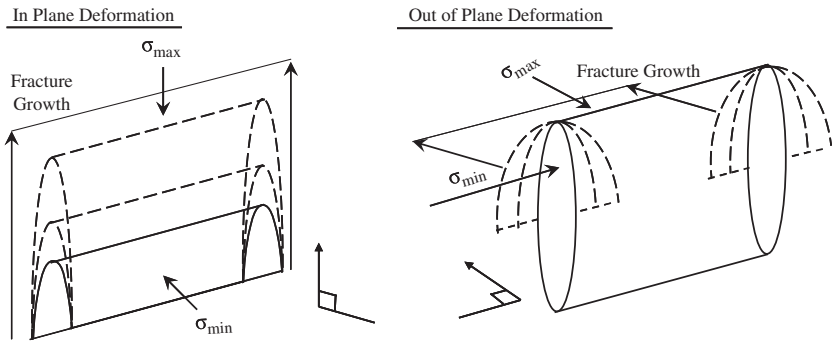


Figure 11. *In situ* stress directions and deformation planes.



DOI: 10.1002/nag

isotropic to highly anisotropic stress field cases. The values of these ratios, namely, are R1, R3.25, R3.5, R3.8, and R4.05. R1 represents the isotropic, whereas R4.05 represents the highly anisotropic case. Table II shows the effective stress field that was considered to ensure in-plane deformation.

As it was found in the previous investigation, the numerical model with the elastic-softening constitutive behavior generates larger plastic zones. For this reason, only the elastic-softening case (weak formation) is considered further in the investigation of the other main parameters.

Figure 12 presents the fracture profile versus distance from wellbore. For comparison reasons, we have left the fractures to propagate up to 3 m enough distance to reach accurate conclusions. We see that the fractures that correspond to the stress ratio R1 (isotropic) to R3.25 (anisotropic) present no difference, and hence, the R1 (isotropic) case is plotted in the figure. In examining the other fractures that correspond to the other stress ratios, it is seen that wider fractures are created when the propagation takes place in a highly anisotropic stress field.

Figure 13 presents the net pressures versus distance from wellbore. It is seen that higher breakdown pressures are needed to initiate the fracture propagation in a highly anisotropic stress field.

Table II. In-plane deformation anisotropic stress field (increase stress deviator).

| $\sigma_1$ (MPa) | $\sigma_3$ (MPa) | $\sigma_2$ (MPa) | Stress deviator ($\sigma_1$–$\sigma_3$) | Plastic zone ($L_p$) | Stress ratio |
|---|---|---|---|---|---|
| 3.7 | 3.7 | 3.7 | 0 | 0 | *R* (1) |
| 12 | 3.7 | 3.7 | 8.3 | 0.599 | *R* (3.25) |
| 13 | 3.7 | 3.7 | 9.3 | 0.626 | *R* (3.5) |
| 14 | 3.7 | 3.7 | 10.3 | 0.650 | *R* (3.8) |
| 15 | 3.7 | 3.7 | 11.3 | 0.671 | *R* (4.05) |

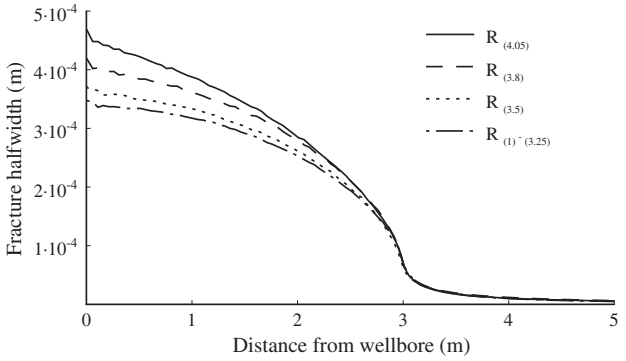


Figure 12. Fracture profiles for different stress ratios.

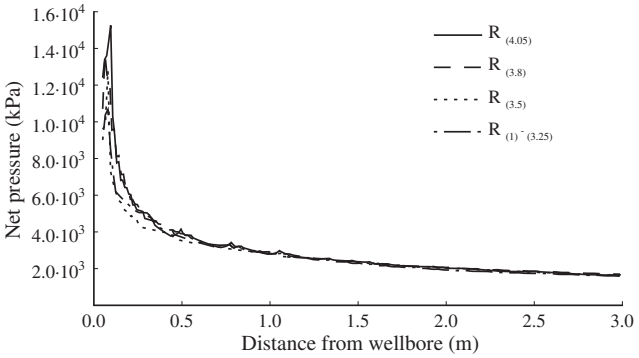


Figure 13. Net pressures for the different stress ratios.



DOI: 10.1002/nag

Figure 14 shows the measure of the plastic dissipation versus time. It is confirmed that almost negligible plastic zones are created when the fracture propagates in an isotropic stress field (R1), and the fracture in this case behaves essentially as poroelastic.

As mentioned earlier, the process zone in poroelastoplastic formations includes both plastic zones and the cohesive zone. In the case of isotropic stress field (R1), the plastic yielding mechanism is not activated; thus, the numerical solution is analyzed in the context of the cohesive zone only. Larger plastic zones are created, and more time is needed to propagate the fractures in a highly anisotropic stress field (R4.05) because of the larger fracture volume that is created.

In all previous investigations presented in this article, we have studied the parameters that are relevant to Equation (20) which is an augmented version of the equation that appeared in publications [12, 15]. Furthermore, we will investigate in this section how the fracture dimensions and fluid pressures depend on the initial pore pressure field. This study can be done with two different types of analysis: (i) with the application of the same effective stress and different pore pressure and (ii) with the application of the same total stress and different pore pressure. In the first set of numerical models, three different values of pore pressures have been applied to correspond to low, intermediate, and high formation pressure. For simplicity, the cases are called pp 0.85, pp 1.85, and pp 2.85 respectively. Table III presents the *in situ* stress field, pore pressure field, and the plastic zone scaling parameter.

The values of pore pressures were added to the effective stresses and the total stress field and pore pressure applied as initial stresses and loading boundary conditions. The computations were carried out with the elastic-softening ($k_n \times 5$) constitutive behavior, which corresponds to soft rock formations.

Figure 15 shows the fracture profiles versus distance from wellbore after all three fractures were left to propagate up to 3 m.

Significantly larger and wider fracture profiles are created when the fractures are driven in high-pressure formations. Figure 16 shows the corresponding fluid pressure profiles for the three cases. We see that higher fluid pressure is needed to split and propagate the fractures in the high-pressure formation. As we can see next, this difference in net pressures is higher for short fractures, but it diminishes as the fracture is getting long and the propagation pressure is controlled by the closure stress.

The visual fracture tip is found to be where the fluid pressure changes sign. Ahead of the three visual fracture tips, the pressure tends to the imposed far-field initial conditions. Figure 16 shows that for a long fracture, the difference in the net pressure for the three cases is equal with the difference in the

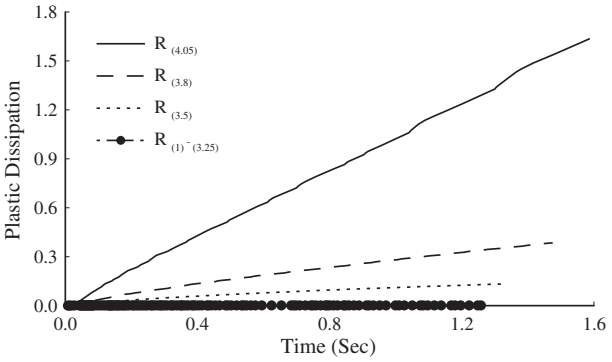


Figure 14. Plastic dissipation versus time for the different stress ratios.

Table III. Influence of pore pressure on the plastic zone scaling.

| $\sigma_1$ (MPa) | $\sigma_3$ (MPa) | $\sigma_2$ (MPa) | Stress deviator ($\sigma_1$–$\sigma_3$) | Plastic zone ($L_p$) | $P$ (MPa) |
|---|---|---|---|---|---|
| 14 | 3.7 | 9 | 10.3 | 0.567 | 2.85 |
| 14 | 3.7 | 9 | 10.3 | 0.487 | 1.85 |
| 14 | 3.7 | 9 | 10.3 | 0.427 | 0.85 |



DOI: 10.1002/nag

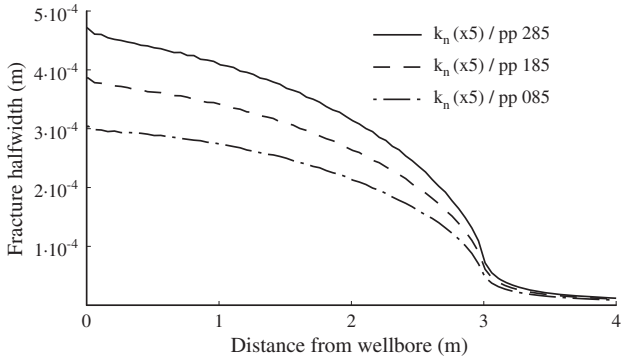


Figure 15. Fracture profiles for the same effective stresses but different values of pore pressures and total stress fields.

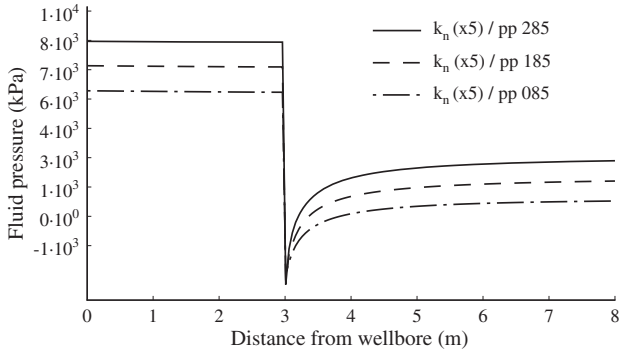


Figure 16. Fluid pressures for the same effective stresses but different values of pore pressures and total stress fields.

initial pore field. For short fractures, the difference in the pressure is larger in the case of high formation pressure due to larger plastic zone, which is created in the high-pressure formation.

This finding is also shown in Figure 17, which presents the net pressures versus distance from wellbore. The net pressure is defined as the pressure in the fracture minus the remote total stress. It is evident that higher net pressures are needed to propagate the short fractures in high-pressure formations. The difference in the three cases decays to zero as the plastic zones scaled with the fracture length become negligible.

Figure 18 presents the measure of plastic dissipation versus time for all three numerical models examined. The last point of each curve corresponds to the time for reaching fracture length of 3 m. It is evident that larger plastic zones are created in the case of the fracture driven in high pressurize

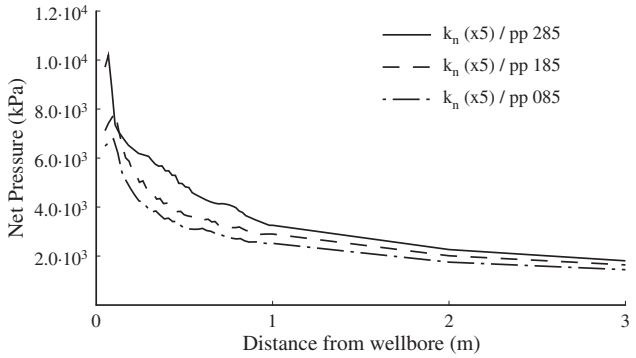


Figure 17. Net pressures for the same effective stresses but different values of pore pressures and total stress fields.



DOI: 10.1002/nag

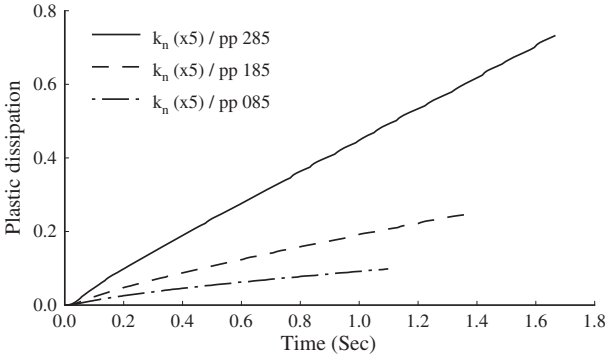


Figure 18. Plastic dissipation for the same effective stresses but different values of pore pressures and total stress fields.

formations. Furthermore, more time is needed for the fracture to reach 3 m length in the high pressure case, of pp 2.85, mainly due to the larger fracture volume that is created.

From the aforementioned analysis, it is concluded that the process zone that includes the plastic zone length $L_p$ is proportional to the initial pore pressure field. In other words, when a fluid-driven fracture is created in a stress field with the same effective stresses but higher pressure formation, the created plastic zone will be larger. Furthermore, development of the plastic zones will result in wider fracture profiles and higher net pressures to propagate a fracture. The importance of the plastic zone that is scaled with the fracture length is diminishing as the fracture gets longer.

As emphasized, the influence of the formation pore pressure can be studied with two different loading cases, with the same effective stress as presented earlier or with the same total stress presented in the following. Analyzing the problem with the same total stress field, it is ensured that the closure stress remains the same. We assumed that the values of the *in situ* stresses presented in Table IV are for effective stresses, and an only small perturbation of pore pressure is varied. Furthermore, we obtain the limiting case of a dry formation by setting the pore pressure equal to zero.

In the next investigation, we have analyzed the problem by imposing as constant values the total stress field and performed numerical simulations with different values of pore pressures (formation pressurization) as initial conditions. These types of boundary and initial conditions enable us to reduce the problem in a dry porous elastoplastic continuum. Figure 19 presents the fracture profile for the three cases examined after the fractures were propagated up to 4 m.

The fracture is narrower in the bulk of the fracture in the case of low-pressure formation as the limiting case of a dry formation. This result is attributed to the backstresses, which tend to close the fracture near the fracture inlet where the diffusion is greater in the case of a low-pressure formation.

Figure 20 presents the corresponding to the aforementioned fluid pressure profiles. It appears that the fracture pressures needed to propagate all fractures are the same. We remind the reader that the closure stress that corresponds to the total stress was kept the same in this computation. The far-field pressures in front of the fracture tend to the imposed boundary value.

From the numerical analysis, it is concluded that a fracture that is driven in a dry porous elastoplastic continuum will have a narrower fracture profile as a result of larger backstresses near the inlet of the fracture. Fractures that are driven in highly pressurized formations will have wider fracture profiles,

Table IV. Influence of pore pressure in the limit of a dry formation.

| $\sigma_1$ (MPa) | $\sigma_3$ (MPa) | $\sigma_2$ (MPa) | Stress deviator ($\sigma_1$–$\sigma_3$) | Plastic zone ($L_p$) | Pore pressure (MPa) |
|---|---|---|---|---|---|
| 14 | 3.7 | 9 | 10.3 | 0.427 | 0.85 |
| 14 | 3.7 | 9 | 10.3 | 0.405 | 0.425 |
| 14 | 3.7 | 9 | 10.3 | 0.386 | 0.0 |



DOI: 10.1002/nag

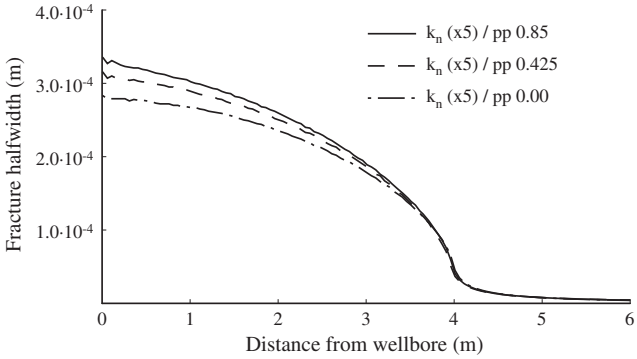


Figure 19. Fracture profiles for the same total stresses but different values of pore pressures and effective stress field.

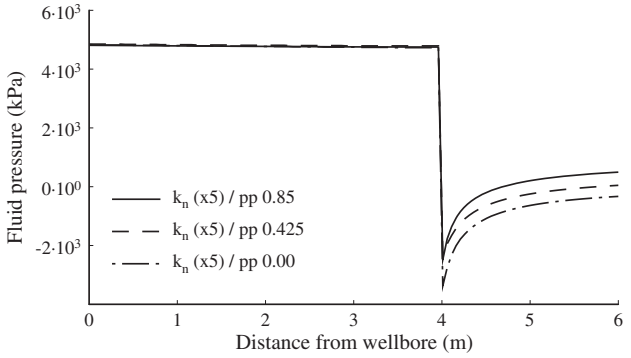


Figure 20. Fluid pressures for the same total stresses but different values of pore pressures and effective stress field.

and higher net pressures will be needed to propagate them mainly due to larger process zone. In both types of analysis (with total and effective stress fields), the plastic zone development is influenced by the pore pressure field. This can be illustrated in the diagram of the Coulomb yield criterion and with the Mohr circle of the stress state. With the introduction of the pore pressure, the Mohr circle is displaced to the left towards the yield criterion, generating larger plastic zones. These plastic zones shield the fracture tip, demanding higher pressures to overcome the energy dissipated in the plastic zones and to fracture the formation, leading to wider fractures and longer pumping time to reach a certain fracture length.

The main focus of this work was to explain at least partially the discrepancy between field observations and predictions by classical hydraulic fracturing simulators in terms of the net pressure needed to propagate the fracture. According to other related research works; this difference is attributed into two main hypotheses. The first hypothesis is that the high observed net pressure is related to a sharp drop of the fluid pressure [35] and to the existence of a dry region near the fracture tip of the fracture [36]. The second hypothesis implies that the nonlinear deformation of the rock might have a strong influence in hydraulic fracturing [13]. In this study, the first hypothesis was dealt with the incorporation of the cohesive zone model as the fracture propagation criterion to ensure that the stresses in the vicinity of the fracture tip will remain finite, and the second hypothesis was investigated by assuming the Mohr–Coulomb yield criterion to deal with plastic yielding with associated dilation. In the following, computations were performed and the results were compared for a fracture driven in porous and nonporous cohesive formations.

Figure 21 presents the fracture opening at wellbore versus time for a fracture driven (i) in a nonporous elastic formation, (ii) in a poroelastic formation and (iii) in a poroelastoplastic formation.



DOI: 10.1002/nag

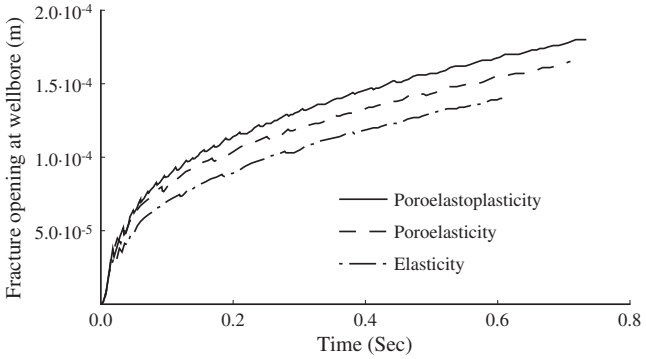


Figure 21. Fracture opening at wellbore for different material behavior.

All three fractures were left to propagate up to 3 m in length. The fracture that is driven in the nonporous elastic formation corresponds to the case of a classical hydraulic fracturing simulator, whereas the fractures that are driven in poroelastic and poroelastoplastic formations correspond to the cases that have been investigated with the advanced model of this study.

Figure 21 shows that the fracture that is driven in a poroelastoplastic formation is wider than the fracture that is driven in poroelastic and nonporous elastic formations. This difference is attributed to the action of the process zone that includes plastic yielding and cohesive zone, as well as due to the influence of the formation pressure and diffusion. For the material and stress data in these computations, the fracture that is driven in a poroelastic formation is 15.2% wider than the fracture driven in nonporous elastic. Furthermore, the fracture that is driven in a poroelastoplastic formation is 22.25% wider than the fracture driven in the nonporous elastic medium.

Figure 22 presents the propagation pressure at wellbore versus time for the three models. It is seen that the pressure needed to propagate the fracture in a poroelastoplastic formation is significantly larger than the pressure needed to propagate the fracture in both poroelastic and nonporous elastic formations. This is explained again by the importance of the process zone that includes plastic yielding and cohesive zone as well the interaction with the formation pressure and diffusion.

A more detail examination of the pressure at wellbore for the specific set of material data that have been used for the computations reveals that the pressure needed to propagate the fracture in a poroelastic formation is 20.9% higher than the pressure needed to propagate the fracture in nonporous elastic formation. Furthermore, the pressure needed to propagate the fracture in a poroelastoplastic formation is 31.8% higher than the pressure needed to propagate the fracture in a nonporous elastic formation. These results are in agreement with the motivation of this work to explain the discrepancy between classical models and field observations.

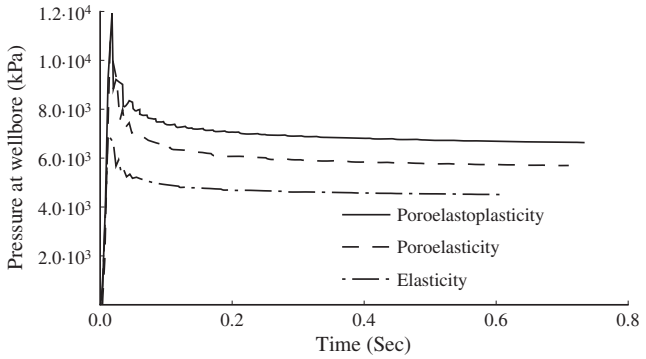


Figure 22. Propagation pressure at wellbore for different material models.



DOI: 10.1002/nag

## 5. CONCLUDING REMARKS

In this study, we analyze some of the main parameters that influence the development of the process zone in fluid-driven fractures in poroelastoplastic domain. These parameters include the cohesive zone characteristics, the *in situ* stress anisotropy, and the formation pressure. The objective was to explain, at least partially, the elevated pressures that are needed to propagate the fractures in the field, and they are not accurately predicted by the conventional models. For this reason, a coupled model that accounts for the fluid flow in the fracture, the rock deformation, and the fracturing processes was developed based on the finite element method. The fractures were driven in a permeable porous elastoplastic domain under plain strain conditions that correspond to weak formation by pumping an incompressible viscous fluid at the fracture inlet. Rock deformation was modeled with the Mohr–Coulomb criterion with an associative flow rule suit for cohesive and frictional materials such as rocks. Fluid flow in the fracture was modeled by lubrication theory, and the movement of the pore fluid in the surrounding medium obeyed the Darcy law. The cohesive zone approach was used as the fracture propagation criterion. The numerical solution yielded the fracture length, the fracture opening and propagation pressure, and the plastic dissipation as a function of the time and distance from the wellbore.

From the analysis conducted, it was found that propagation with an elastic-softening cohesive model, instead of rigid softening, yields larger plastic zones, which results in higher propagation pressure and wider fractures. These results are due to the larger process zone, which includes both the cohesive zone and the plastic zones. Furthermore, we showed that in the poroelastoplastic continuum the cohesive and dilatant regions near the tip enforce suction. This pore fluid flux is even greater in the case of a fluid-driven fracture in weak rock formation, suggesting that plastic dilation increases the fluid flux.

The *in situ* anisotropic stress field creates larger plastic zones, leading to wider fracture profiles and higher propagation pressures. These obtained computations are a direct result of the large stress deviator that was considered in this case. When fracture propagation takes place in isotropic or in small stress deviator field, the formation behaves essentially as poroelastic.

Fluid-driven fractures in high-pressure formations result in wider fractures and higher propagation pressures as a consequence of the larger plastic zone development. Furthermore, the fracture fluid diffusion enters in the process, creating backstresses at the inlet and bulk of the fracture.

ACKNOWLEDGEMENTS

The authors acknowledge the International Water Research Center NIREAS (NEA IPODOMI/STRATH II/0308/09), cofunded by the Republic of Cyprus and the European regional development fund.

REFERENCES

1. Desroches J, Detournay E, Lenoach B, Papanastasiou P, Pearson JRA, Thiercelin M, Cheng A. The crack tip region in hydraulic fracturing. *Proceedings of the Royal Society of London* 1994; **44**:39–48.
2. Carbonell R, Desroches J, Detournay E. A comparison between a semi-analytical and a numerical solution of a two – dimensional hydraulic fracture. *International Journal of Solids and Structures* 1999; **36**:4869–4888.
3. Garagash DI, Detournay E. Plain strain propagation of fluid driven fracture: small toughness solution. *ASME Journal of Applied Mechanics* 2005; **72**:916–928.
4. Savitski A, Detournay E. Propagation of a fluid-driven penny-shape fracture in an impermeable rock: Asymptotic solutions. *International Journal of Solids and Structures* 2001; **39**:6311–6337.
5. Detournay E. Propagation regimes of fluid driven fractures in impermeable rocks. *International Journal of Geomechanics* 2004; **1**:1–11.
6. Zhang X, Detournay E, Jeffrey R. Propagation of a penny-shape hydraulic fracture parallel to the free-surface of an elastic half-space. *International Journal of Fracture* 2002; **115**:125–158.
7. Lecampion B, Detournay E. An implicit algorithm for the propagation of a hydraulic fracture with a fluid lag. *Computer Methods in Applied Mechanics and Engineering* 2007; **196**:4863–4880.
8. Adachi J, Detournay E. Plain strain propagation of a hydraulic fracture in permeable rock. *Engineering Fracture Mechanics* 2008; **75**:4666–4694.
9. Van Dam DB, Papanastasiou P, De Pater CJ. Impact of rock plasticity on hydraulic fracture propagation and closure. *SPE Production & Facilities* 2002; **17**:149–159.
10. Biot MA. General theory of three dimensional consolidation. *Journal of Applied Physics* 1941; **12**:155–164.



DOI: 10.1002/nag

11. Van Den Hoek PJ, Van Den Berg JTM, Shlyapobersky J. Theoretical and experimental investigation of rock dilatancy near the tip of a propagating hydraulic fracture. *International Journal of Rock Mechanics, Mining Sciences and Geomechanical Abstracts* 1993; **30**:1261–1264.
12. Papanastasiou P, Thiercelin M. Influence of inelastic rock behavior in hydraulic fracturing. *International Journal of Rock Mechanics, Mining Sciences and Geomechanical Abstracts* 1993; **30**:1241–1247.
13. Papanastasiou P. The influence of plasticity in hydraulic fracturing. *International Journal of Fracture* 1997; **84**:61–79.
14. Papanastasiou P. An efficient algorithm for propagating fluid driven fractures. *Computational Mechanics* 1999a; **24**:258–267.
15. Papanastasiou P. The effective fracture toughness approach in hydraulic fracturing. *International Journal of Fracture* 1999b; **96**:127–147.
16. Bigoni D, Radi E. Mode I crack propagation in elastic–plastic pressure-sensitive materials. *International Journal of Solids and Structures* 1993; **30**:899–919.
17. Radi E, Bigoni D, Loret B. Steady crack growth in elastic–plastic fluid saturated porous media. *International Journal of Plasticity* 2002; **18**:345–358.
18. Boone TJ, Wawrzynek PA, Ingraffea AR. Simulation of fracture process in rock with application to hydrofracturing. *International Journal of Rock Mechanics, Mining Sciences and Geomechanical Abstracts* 1986; **23**:255–265.
19. Boone JT, Ingraffea AR. A numerical procedure for simulation of hydraulically driven fracture propagation in poroelastic media. *International Journal for Numerical and Analytical Methods in Geomechanics* 1990; **14**:27–47.
20. Schrefler BA, Secchi S, Simoni L. On adaptive refinement techniques in multi-field problems including cohesive fracture. *Computional Methods in Applied Mechanics and Engineering* 2006; **195**:444–461.
21. Sarris E, Papanastasiou P. The influence of cohesive process zone in hydraulic fracturing modelling. *International Journal of Fracture* 2011a; **167**:33–46.
22. Sarris E, Papanastasiou P. Modelling of hydraulic fracturing in a poroelastic cohesive formation. *International Journal of Geomechanics* 2011b. doi:10.1061/(ASCE)GM.1943-5622.0000121.
23. Lhomme TPY. Initiation of Hydraulic Fractures in Natural Sandstones. *PhD Thesis*, TU Delft, Netherlands, 2005.
24. Rice JR, Cleary MP. Some basic stress diffusion solutions for fluid-saturated elastic porous media with compressible constituents. *Reviews of Geophysics and Space Physics* 1976; **14**:227–241.
25. Fjaer E, Holt RM, Horsrud P, Raaen AM, Risnes R. *Petroleum Related Rock Mechanics. Developments in Petroleum Science*. Elsevier: New York, 1996.
26. Rice JR. A path independent integral and the approximate analysis of strain concentration by notches and cracks. *Journal of Applied Mechanics* 1968; **57**:379–386.
27. Kanninen MF, Popelar CH. *Advanced fracture mechanics*. Oxford University Press: UK, 1985.
28. Hillerborg A, Modeer M, Petersson PE. Analysis of crack formation and crack growth in concrete by means of fracture mechanics and finite elements. *Cement and Concrete Research* 1976; **6**:773–782.
29. Lewis RW, Schreffler BA. *The Finite Element Method in the Static and Dynamic Deformation and Consolidation of Porous Media*. John Wiley and Sons: New York, 2000.
30. Shet C, Chandra N. Analysis of energy balance when using cohesive zone models to simulate fracture processes. *Journal of Engineering Materials and Technology* 2002; **124**:440–450.
31. Abaqus Version 6.6 Manuals, 2006.
32. Sinclair GB. On the influence of cohesive stress-separation laws on elastic stress singularities. *Journal of Elasticity* 1996; **44**:203–221.
33. Zuorong C, Bunger AP, Zhang X, Jeffrey RJ. Cohesive zone finite element-based modeling of hydraulic fractures. *Acta Mechanica Solida Sinica* 2009; **22**:443–452.
34. Loret B, Prevost JH. Dynamic strain localization in fluid-saturated porous media. *Journal of Engineering Mechanics* 1991; **117**:907–922.
35. Detournay E. Fluid and solid singularities at the tip of a fluid-driven fracture. In *Proc. IUTAM Symposium on Non-Linear Singularities in Deformation and Flow*, Durban D, Pearson JRA (eds.). Kluwer Academic Publishers: Dordrecht, NL, 1998.
36. Garagash D. Propagation of plane-strain hydraulic fracture with a fluid lag: Early-time solution. *International Journal of Solids and Structures* 2006; **46**:5811–5835.




DOI: 10.1002/nag